# Metabolic imaging using hyperpolarized pyruvate-lactate exchange assesses response or resistance to the EGFR inhibitor cetuximab in patient-derived HNSCC xenografts

Lionel Mignion[1], Stefania Acciardo[1], Florian Gourgue[1,6], Nicolas Joudiou[2], Xavier Caignet[3], Rose-Marie Goebbels[3], Cyril Corbet[4], Olivier Feron[4], Caroline Bouzin[5], Patrice D. Cani[6], Jean-Pascal Machiels[3], *Sandra Schmitz[3], *Bénédicte F. Jordan[1]

[1]Biomedical Magnetic Resonance Research Group, Louvain Drug Research Institute, UCLouvain, Université Catholique de Louvain, Brussels, Belgium

[2]Nuclear and Electron Spin Technologies Platform (NEST), Louvain Drug Research Institute, UCLouvain, Université Catholique de Louvain, Brussels, Belgium

[3]Institut Roi Albert II, Service d'Oncologie Médicale, Cliniques universitaires Saint-Luc and Institut de Recherche Expérimentale et Clinique, UCLouvain, Université Catholique de Louvain, Brussels, Belgium

[4]Pole of Pharmacology and Therapeutics (FATH), Institut de Recherche Expérimentale et Clinique (IREC), Université catholique de Louvain, 53 Avenue Mounier B1.53.09, Brussels, B-1200, Belgium.

[5]Imaging platform 2IP, Institut de Recherche Expérimentale et Clinique, UCLouvain, Université Catholique de Louvain, Brussels, Belgium

[6]Metabolism and Nutrition Group, Louvain Drug Research Institute, UCLouvain, WELBIO (WELBIO- Walloon Excellence in Life Sciences and BIOtechnology), Université Catholique de Louvain, Brussels, Belgium

*contributed equally to this work as last author

Running title: Metabolic imaging identifies HNSCC sensitivity to cetuximab.

**Corresponding author:**
Bénédicte F. Jordan, PhD
UCLouvain, Louvain Drug Research Institute**,**
Biomedical Magnetic Resonance Group
Av. Mounier 73.08, 1200 Brussels, Belgium
Benedicte.jordan@uclouvain.be

Conflict of interest: there is no conflict of interest to declare.

**Abstract**

Optimal Head and Neck Squamous Cell Carcinoma (HNSCC) patient selection for anti-EGFR-based therapy remains an unmet need since only a minority of patients derive long-term benefit from cetuximab treatment. We assessed the ability of state-of-the art non-invasive *in vivo* metabolic imaging to probe metabolic shift in cetuximab-sensitive and resistant HNSCC patient-derived xenografts (PDTX).

Methods: Three models selected based on their known sensitivity to cetuximab in patients (cetuximab-sensitive or acquired-resistant HNC007 PDTX, cetuximab-naïve UCLHN4 PDTX, and cetuximab-resistant HNC010 PDTX), were inoculated in athymic nude mice.

Results: Cetuximab induced tumor size stabilization in mice for 4 weeks in cetuximab-sensitive and naïve models treated with weekly injections (30mg/kg) of cetuximab. Hyperpolarized $^{13}$C-pyruvate - $^{13}$C-lactate exchange was significantly decreased *in vivo* in cetuximab-sensitive xenograft models 8 days after treatment initiation, whereas it was not modified in cetuximab-resistant xenografts. *Ex vivo* analysis of sensitive tumors resected at day 8 post-treatment highlighted specific metabolic changes, likely to participate in the decrease in the lactate to pyruvate ratio *in vivo*. Diffusion MRI showed a decrease in tumor cellularity in the HNC007 sensitive tumors, but failed to show sensitivity to cetuximab in the UCLHN4 model.

Conclusion: This study constitutes the first *in vivo* demonstration of cetuximab-induced metabolic changes in cetuximab-sensitive HNSCC PDTX that were not present in resistant tumors. Using metabolic imaging, we were able to identify hyperpolarized $^{13}$C-pyruvate as a potential marker for response and resistance to the EGFR inhibitor in HNSCC.

Keywords: Head & Neck PDTX, Cetuximab, $^{13}$C-MRS, [1-$^{13}$C]pyruvate, Diffusion imaging.

**Translational relevance**

Cetuximab, an EGFR inhibitor, improves overall survival in squamous cell carcinoma of the head and neck (HNSCC). However, only a minority of patients derive long-term benefit from this compound and, to date, no predictive biomarkers able to select patients for anti-EGFR therapies have been validated for HNSCC. We assessed the ability of state-of-the art non-invasive *in vivo* metabolic imaging to probe the metabolic shift in cetuximab-sensitive and resistant HNSCC patient-derived xenografts (PDTX). We identified hyperpolarized $^{13}$C-pyruvate/$^{13}$C-lactate exchange as a potential marker for response and resistance to the EGFR inhibitor in 3 distinct HNSCC PDTX models in mice. Along with the recent implementation of hyperpolarized metabolic imaging in the clinical setting, the current work suggests the potential relevance of hyperpolarized $^{13}$C-pyruvate to monitoring therapy response in HNSCC patients in the transition towards personalized therapy.

## Introduction

Overexpression of the Epidermal Growth Factor Receptor (EGFR) in squamous cell carcinoma of the head and neck (HNSCC) is associated with poor prognosis, radioresistance, and chemoresistance (1,2). Cetuximab is a chimeric IgG1 monoclonal antibody (mAb) that specifically binds to the EGFR with high affinity and improves overall survival when associated with radiation therapy in locally advanced HNSCC, or with platinum-based chemotherapy in incurable disease (3,4). However, only a minority of patients derive long-term benefit from anti-EGFR mAbs (5,6). Resistance mechanisms to EGFR inhibition for HNSCC remain unclear (7), although multiple mechanisms of acquired and de novo resistance have been suggested (8,9), paving the way for trials of combination strategies (10-12). Optimal HNSCC patient selection for anti-EGFR-based therapy remains a challenge (7). Even though initial approval for the clinical use of cetuximab was based on EGFR overexpression in primary or metastatic tumors (13), EGFR mutations, protein expression or copy number are not considered relevant in making decisions on the use of EGFR inhibitors in several cancer types (14-17). In this context, early prediction of treatment sensitivity or resistance to EGFR inhibitors could spare patients from futile therapy cycles and unnecessary side effects.

Conventional anatomically-based endpoints may be inadequate to monitor tumor response to targeted agents that usually do not result in tumor shrinkage but rather in tumor size stabilization. Imaging methods exploit the altered metabolism in treatment-responsive tumors as a method for the evaluation of treatment response (18). Within this scope, an early $^{18}$FDG-PET response has been associated with anti-EGFR therapy outcome in lung and colorectal cancer (19-21). A recent PET preclinical study has revealed higher relative uptake of $^{18}$F-FDG in multiple Tyrosine-Kinase (TK) resistant HNSCC patient-derived tumor xenografts (PDTX) in mice (22). Our group, however, showed that SUVmax, if modified in response to cetuximab, was not always able to discriminate between cetuximab-sensitive and resistant PDTX in multiple models (23). In addition, EGFR phosphorylation was decreased in both sensitive and resistant PDTX, showing that pEGFR quantification cannot be used as a marker of resistance to cetuximab (23).

A limited number of studies have focused on the effect of EGFR inhibitors on tumor metabolism in order to identify potential resistance mechanism pathways. Based on the fact that tumor cell proliferation was not systematically decreased in response to EGFR inhibition in multiple HNSCC cell line studies, Liu et al. observed that inhibition of glycolysis via LDH-A downregulation was required for cetuximab to induce antiproliferative effects, whereas resistant cells were highly glycolytic (24). Activated protein kinase AMPK was further shown to be transiently increased in response to glycolysis inhibition, helping cancer cells to restore energy homeostasis and survive cetuximab-induced inhibition of glycolysis (25). Finally, phosphorylation (inhibition) of acetyl-CoA carboxylase (ACC) following AMPK activation was shown to be followed by a compensatory increase in total ACC, rewiring the HNSCC tumor metabolism from glycolysis-dependent to lipogenesis-dependent (26).

The goal of the current study was to assess the ability of state-of-the art non-invasive *in vivo* metabolic imaging to probe metabolic shifts in cetuximab-sensitive and resistant HNSCC xenografts derived from three HNSCC patients. One was sensitive to cetuximab treatment, with its acquired resistant counterpart being generated in mice, one showed resistance to the EGFR inhibitor, and one was also sensitive to cetuximab, thereby constituting good models for assessing the relevance of hyperpolarized $^{13}$C-pyruvate-lactate exchange as a potential marker for response and resistance to cetuximab treatment. Hyperpolarization of $^{13}$C-enriched metabolites increases $^{13}$C-magnetic resonance spectroscopy (MR) sensitivity by a factor of 10,000, allowing *in vivo* real time assessment of metabolic fluxes (27). This state-of-the-art metabolic imaging method is currently used to assess tumor metabolism and treatment sensitivity in preclinical studies (28,29), and was also recently translated to the clinical setting (30,31). Pyruvate is the product of glycolysis and can be assessed using hyperpolarized (HP) MRI. In particular, [1-$^{13}$C]pyruvate is reduced to [1-$^{13}$C]lactate via the enzyme lactate dehydrogenase (LDH). This process results in an altered chemical shift that HP MRI can image at uniquely high temporal resolution (32). In addition, we used diffusion imaging to monitor cellularity (tumor cell density) *in vivo*, before and after treatment with cetuximab. DW-MRI has been used to detect early changes after standard or targeted therapies (33-35). Cell death in response to therapies

can precede size change and increases the mobility of water molecules in the tissue environment. DW-MRI may therefore be an early biomarker for response since its measurable parameter ADCw (Apparent Diffusion Coefficient of water) assesses tumor cellularity. In this way, both metabolic ($^{13}$-C pyruvate to $^{13}$C-lactate conversion) and cell viability (ADCw) *in vivo* markers provide complementary information with respect to sensitivity or resistance to the EGFR inhibitor. *In vivo* imaging data were compared with *ex vivo* mRNA expression, protein levels or IHC staining of enzymes and transporters involved in the glycolytic pathway. Finally, correlation with IHC staining for pEGFR was performed in control and treated cetuximab-sensitive and cetuximab-resistant tumors.

## Materials and methods

### Generation of PDTX models

HNC007 and HNC010 PDTX models were established in collaboration with Trace, the PDTX platform of KU Leuven (www.uzleuven-kuleuven.be/lki/trace), as previously described (23). A UCLHN4-cetuximab sensitive PDTX model was established in the medical oncology group at UCLouvain. All PDTX models were derived from patients with HNSCC. The study was approved by the local ethical committees (UCL/MD/2012/09July/314) in accordance with the principles of the Declaration of Helsinki and all patients gave their written informed consent. Patient tumor materials were collected in RPMI medium (Gibco, Waltham, MA, USA) supplemented with 0.4% fungizone (Bristol Myers Squibb, New-York, USA), Pen/Strep 2.5% (Sigma, St Louis, Missouri, USA), and gentamycin (Braun Medical, Bethlehem, Pennsylvania, USA), and kept at 4°C for engraftment within six hours of resection. Necrotic and supporting tissues were carefully removed using a surgical blade. Some tumor fragments were flash frozen and stored at −80° C for genomic profiling, and other fragments were fixed in 4% neutral-buffered formalin and paraffin embedded for histopathologic analysis. The remaining tumor fragments were implanted subcutaneously into the backs of of 4-6 weeks (22-25g) athymic nude female mice (NMRI-Foxn1nu, Taconic, NY, USA). Successfully engrafted tumor models were then passaged through several generations. Experiments were

conducted on the fifth and sixth generations. All PDTX models were validated by comparing the clinical behavior (sensitivity to cetuximab) and immunochemistry (p16 (clone G175-405, BD Pharmingen, CA, USA); Ki67 (polyclonal rabbit, Thermo Fisher Scientific, Waltham, MA USA); p53 (clone SP5, Thermo Fisher Scientific, Waltham, MA USA); pEGFR (clone 7A5, Cell Signaling Technology, MA, USA); vimentin (clone SP20, Thermo Fisher Scientific, Waltham, MA USA), and E-Cadherin (clone 24E10, Cell Signaling Technology, MA, USA))) of the primary tumor with the tumors harvested from fourth- and sixth-generation mice. EGFR was not mutated in the PDTX models under study, as assessed by WES (whole exome sequencing) analysis. Some mice from the initial HNC007 model were treated with cetuximab (30 mg/kg, once a week intraperitoneally) until some became resistant to cetuximab. Resistance was defined as continuous tumor growth under cetuximab and an increase in tumor volume of more than 200% compared with baseline. Mice were maintained and handled in accordance with the UCLouvain policy for animal care. Animal work was undertaken in compliance with Belgian law and all the experiments were conducted in accordance with our local ethical committee. Animal welfare is regularly controlled by inspections in compliance with Belgian law, and all investigators performing animal work successfully completed FELASA C training. Tumor bearing mice were randomly assigned to the cetuximab-treated and vehicle groups.

**Treatment**

Cetuximab-sensitive and resistant HNSCC bearing mice were treated intraperitoneally with cetuximab (Merck Serono, Darmstadt, Germany) at a dose of 30 mg/kg, as described previously (23). Two doses of cetuximab were given; the first was administered just after the initial MR assessments at baseline (day 0), and the second followed one week later on day 7. Post-treatment MR experiments were performed on day 8. The vehicle (saline solution) was administered to the control groups under the same conditions. Mice were distributed randomly

in the control or cetuximab group. To evaluate treatment effects, tumor size was first measured by caliper once a week and tumor volume was calculated according to the equation: $V(mm^3)$ = (the greatest length)×(the shortest length)$^2$/2 (Fig.1A and 1D). During MR experiments, tumor size was measured on the basis of anatomical $T_2$ images.

**MR experiments**

MR experiments were performed in an 11.7-Tesla, 16-cm inner diameter system (Bruker, Biospec, Ettlingen, Germany) equipped with a $^1$H-quadrature volume coil (40-mm inner diameter) and a double tuned $^1$H-$^{13}$C-surface coil (RAPID Biomedical), as described previously (23). Mice were anesthetized by isoflurane inhalation (2.5% in air for induction and 1–2% in air for maintenance). Body temperature was maintained using a warm circulating water blanket and monitored using a rectal temperature probe. A pressure cushion was used to monitor breathing. Anatomical $T_2$-weighted images were used to assess tumor volume. The turbo RARE sequence had the following parameters: repetition time (TR) = 2.5s, echo time (TE) = 30 ms, averages = 2, field of view = 3 × 3 cm, 15 slices with a 1 mm thickness. For Diffusion-MRI, a transverse echo planar imaging sequence was used with the following parameters: TR/TE = 3000/27 ms, duration of diffusion gradients $\delta$ = 7 ms, separation of diffusion gradients ($\Delta$) = 14ms, slice number = 7, slice distance = 1 mm, *b*-values = 100–200–400–600–800–1000 s/mm$^2$, acquisition time = 4 min 12 sec. Mean apparent diffusion coefficients (ADC) were extracted from DW images and averaged for every slice of tumor using Matlab software (The MathWorks Inc., Natick, MA, USA). A second anatomical $T_2$-weighted image was acquired with geometrical parameters similar to those of the Diffusion Weighted-MRI scan to allow co-registration of the diffusion map with anatomical images. The exponential decay of the signal as a function of the b-value was measured according to the Stejskal–Tanner equation. ADC maps were generated by nonlinear least squares regression of a mono-exponential to the experimental signal intensity for all *b* values.

## Hyperpolarized $^{13}$C-NMR spectroscopy and data analysis

Hyperpolarized 13C-NMR data were acquired as previously described (36). [1-$^{13}$C] pyruvic acid (Sigma-Aldrich) was mixed with 15 mM trityl radical OX63 and doped with 2 mM gadoteric acid (Guerbet). This solution of 40 µl was hyperpolarized by an Oxford DNP Polarizer (HyperSense) for approximately 45 min at 1.4 K and 3.35 T. The polarized substrate was quickly dissolved in 3 ml of heated buffer containing 100 mg/l EDTA, 40 mM HEPES, 30 mM NaCl, and 80 mM NaOH. The final solution was adjusted to have a neutral pH and contained hyperpolarized [1-$^{13}$C] pyruvate and non-hyperpolarized, unlabeled lactate (30 mM) to increase $^{13}$C label exchange (36). This solution was quickly injected using a catheter into the tail vein of the mice in the MRI scanner (11.7-Tesla, Bruker, Biospec). Mice were scanned using a double tuned $^{1}$H-$^{13}$C-surface coil (RAPID Biomedical) which was designed for spectroscopy of subcutaneous tumors (i.e., tumor-shaped cavity of 12 mm in diameter). After administration of 0.2 mL of hyperpolarized pyruvate, $^{13}$C spectra were acquired using a single pulse sequence every 3 sec for 210 sec (70 repetitions), a flip angle of 10° and an acquisition bandwidth of 50 kHz (10000points). Peak areas under the curve were measured for each repetition time and each time point using homemade routines in MATLAB (Mathworks). The integrated peak intensities of hyperpolarized $^{13}$C-pyruvate, $^{13}$C-lactate, and $^{13}$C global signal were measured. The rate of exchange between pyruvate and lactate was calculated.

## pEGFR Immunohistochemistry (IHC)

pEGFR IHC (clone 7A5, Cell Signaling Technology, MA, USA) was performed on 4-µm paraffin-embedded tumor sections. Slides were scanned (Leica SCN400 Slide Scanner, Leica Biosystems, Germany) and digitalized at X20 magnification. The slides were analyzed using TissueIA software (Leica Biosystems, Dublin, Ireland). The quantification algorithm was run

in the pre-selected viable part of the tissue samples to detect stained area and tissue area. The histoscore is calculated as follows: histoscore = (positive area* average staining intensity)/(total tissue area). The presented results are normalized to the mean of the control group.

**Tumor mRNA analysis**

Frozen tumor tissues were ground with a pestle in liquid nitrogen to obtain homogeneous tissue powder. The total RNA was isolated from the tumor powder using the TriPure Isolation Reagent (Roche Diagnostics). cDNA was prepared by reverse transcription using the GoScript Reverse Transcriptase System (Promega, Madison, WI, USA). Real-time PCR was performed using a QuantStudio 3 Real-Time PCR system (ThermoFisher Scientific), using Mastermix Plus for SYBR Assay (Eurogentec, Liège, Belgium). Data were analyzed using the $2^{-\Delta\Delta}$CT method. The Glyceraldehyde-3-Phosphate Dehydrogenase (GAPDH) gene was chosen as a reference gene. Primer sequences are listed in Supplementary Data.

**Western-blot analyses**

Homogeneous tumor powder were lysed in RIPA buffer (Sigma) supplemented with 1% of Halt protease inhibitors and Halt phosphatase inhibitors (ThermoFisher). Equal amounts of proteins were separated by SDS–PAGE and transferred to PVDF membranes. Membranes were incubated overnight at 4°C with antibodies diluted in Tris-buffered saline tween-20 containing 1% bovin serum albumin. The revelation was performed using a chemiluminescent substrate (SuperSignal® West Pico ThermoScientific) and LAS 500 (GE Healthcare). Densitometry analysis was performed with ImageQuanTL software.

**Statistics**

The two primary endpoints of this study aimed to determine (i) whether the imaging parameters experienced significant changes between baseline and day 8 and (ii) whether these changes differed between the cetuximab-treated groups versus the untreated group in both sensitive and resistant models at day 8.

All analyses were performed using GraphPad Prism 7 software, as described previously (23). In the HNC007 model, data at baseline and day 8 were compared using a paired samples *t*-test. Comparisons of changes in tumor size and in imaging parameters (normalized to their baseline values) between control, sensitive, and resistant groups in HNC007 model were carried out using a two-way ANOVA test followed by a Tukey post-hoc test for group comparisons. For UCLHN4 and HNC010 models including only two groups, 1-way ANOVA with multiple comparison post-tests were performed (Sidak for the comparison between control and treated group, and the two-stage linear step-up procedure of Benjamini, Krieger and Yekutieli for the D0-D8 comparison). The pEGFR IHC data were analyzed using one-way ANOVA (Kruskal-Wallis test). Finally, the mRNA expression was compared between groups using one-way ANOVA with Tukey's multiple comparison post-hoc tests or Welch's test where appropriate. For all tests cited above, a $p$-value $< 0.05$ was considered statistically significant.

**Results**

Tumor growth was stabilized for 5 weeks under weekly treatment with 30 mg/kg IP injections of cetuximab in the HNC007 cetuximab-sensitive patient-derived tumor xenografts, in contrast to the vehicle-treated xenografts (Fig.1A, p=0.0002, ANOVA 2-way, n=6-9/group). During the 8 days of our metabolic imaging study, tumor growth was not significantly modified with respect to pre-treatment tumor volume in the control (Fig.1 B) and cetuximab-sensitive (Fig.1 C) treated groups, although a trend toward an increase was already present in

the control group (Fig.1 B&C, n=3/4 group, paired t-test, p=0.07 and 0.16 respectively). Fig.1 C confirms the tumor size stabilization induced by cetuximab while comparing tumor size at D0 and D8. However, the limited number of animals in Fig.1C does not allow a definitive conclusion to be drawn about the potential ability of cetuximab to decrease tumor size between D0 and D8. Nevertheless, statistics performed on the larger cohort used in Fig.1A for tumor growth assay show a lack of reduction in tumor size in the cetuximab-treated group between D0 and D7, and ANOVA comparison between control and treated groups does not show any significant difference between control and cetuximab groups on D7, but only on D14. Resistance to cetuximab was induced *in vivo* in HNC007 mice-bearing xenografts. Xenografts were considered resistant when tumors reached 200% +/- 10% of their initial size (Fig.1D, n=4). In this group, no significant change in tumor volume was observed within the 8 days of the metabolic imaging study (Fig.1E, n=4, paired t-test, p=0.28). Accordingly, the evolution of tumor volume between day 0 and day 8 (normalized to pre-treatment volume on day 0) was significantly different for control and cetuximab-sensitive treated groups (Fig. 1F, p=0.05, n=3/4 group, 2-way ANOVA, Sidak multiple comparison test), but not for control xenografts and cetuximab-resistant treated xenografts (Fig.1F, p=0.51, n=3/4 group, 2-way ANOVA, Sidak multiple comparison test).

EGFR phosphorylation quantified by IHC was significantly decreased in cetuximab-sensitive HNC007 xenografts on day 8 after weekly treatment with cetuximab, but not in cetuximab-resistant xenografts, in comparison with vehicle-treated xenografts (Fig.2, n=3-4/group, Kruskal-Wallis test, p=0.04).

Real time pyruvate-lactate exchange after IV administration of hyperpolarized $^{13}$C-pyruvate (Fig.3A) was assessed by calculating the area-under-the curve (AUC) of the dynamic acquisitions of lactate and pyruvate peaks over time (Fig.3B). The calculated $^{13}$C-lactate to $^{13}$C-pyruvate ratio was not modified in control xenografts between pre-treatment (day 0) and

post-treatment (day 8) (p=0.37, n=3; paired t-test, Fig.3C), or in cetuximab-resistant HNC007 xenografts (p=0.38, n=4, paired t-test, Fig.3D); whereas it significantly decreased in cetuximab-sensitive HNC007 xenografts (p=0.004, n=3; paired t-test, Fig.3E). There was therefore a significant difference in the evolution of the ratios between day 0 and day 8 (Fig.3F) for control and sensitive treated xenografts (p=0.0003, n=3/4 group; 2-way ANOVA, Sidak multiple comparison test) and for sensitive and resistant xenografts (p=0.03, n=3/4 group, 2-way ANOVA, Sidak multiple comparison test). In conclusion, cetuximab-sensitive xenografts showed a decreased pyruvate to lactate exchange within one week of treatment, unlike cetuximab-resistant xenografts. $^{13}$C-pyruvate lactate exchange allowed sensitive and resistant xenografts to be distinguished. Of note, the times to maximum peak of the signals after tracer injection were not significantly different before and after treatment with cetuximab in HNC007 sensitive and resistant xenografts (p=1.00 and p=0.39 respectively). These observations indicate that the delivery of hyperpolarized substrates was not likely to be modified by treatment with cetuximab.

Changes in tumor cellularity were measured using the apparent diffusion coefficient of water (ADCw) via Diffusion-MRI (Fig.4). Typical tumor ADCw maps overlaid on anatomical $T_2$ images of xenografts at day 0 and 8 are shown in Fig.4 A&B, respectively. Tumor ADCw had a tendency to increase in control xenografts (Fig.4C, p=0.051, n=4) and significantly increased in response to cetuximab in the HNC007 cetuximab-sensitive group (Fig.4D, p=0.049, n=3, paired t-test). The resistant group, however, showed a significant decrease (Fig.4E, p=0.033, n=4) in tumor ADCw. In conclusion, the ADCw coefficient allowed sensitive and resistant xenografts (Fig.4F, n=3/4 group, p=0.005, 2-way ANOVA, Sidak multiple comparison test) to be distinguished, but not control and cetuximab-sensitive treated xenografts (Fig.4F, n=3/4 group, p=0.35, 2-way ANOVA, Sidak multiple comparison test).

As detailed in the methods section, xenografts were also generated from a second cetuximab-sensitive HNSCC tumor patient (UCLHN4) and from a cetuximab-resistant tumor patient (HNC010) (Fig.5). In UCLHN4 cetuximab-sensitive xenografts (Fig.5A), the evolution of the tumor size between day 0 (pre-treatment) and day 8 (post-treatment), although not significantly different within each individual group when compared to pre-treatment values on day 0, was slightly opposite in control (vehicle-treated) and cetuximab-treated xenografts (Fig.5A, p=0.04, n=5/7 group; 2-way ANOVA, Sidak multiple comparison test). In HNC010 cetuximab-resistant xenografts (Fig.5B), the evolution of the tumor size between day 0 and day 8 was not significantly different for control and treated tumors (Fig.5B, p=0.57, n=5/6 group; 2-way ANOVA, Sidak multiple comparison test). In UCLHN4 cetuximab-sensitive xenografts (Fig.5C), $^{13}$C-lactate to $^{13}$C-pyruvate exchange was not modified in control xenografts (Fig.5C, p=0.33 , n=4, 2-way ANOVA, two-stage linear step-up procedure of Benjamini, Krieger and Yekutieli), but was significantly decreased between pre- and post-treatment with cetuximab (Fig.5C, p=0.04, n=6, 2-way ANOVA, two-stage linear step-up procedure of Benjamini, Krieger and Yekutieli). In HNC010 cetuximab-resistant xenografts (Fig.5D, n=5/6 group), however, no change in the $^{13}$C-lactate to $^{13}$C-pyruvate ratio was observed in both control and cetuximab-treated groups. In UCLHN4 cetuximab-sensitive xenografts, the ADCw coefficient allowed control and treated xenografts to be distinguished (Fig.5E, p=0.04, n=5/7 group; 2-way ANOVA, Sidak multiple comparison test) due to the significant decrease in the ADCw in the control group (Fig.5E, p=0.02, n=5, 2-way ANOVA, two-stage linear step-up procedure of Benjamini, Krieger and Yekutieli). In HNC010 cetuximab-resistant xenografts (Fig.5F, n=5/6 group), no change in ADCw was observed in either group. EGFR phosphorylation was significantly decreased in cetuximab-sensitive UCLHN4 xenografts at day 8 after cetuximab treatment (Fig.5G, p=0.02 n=6/7 group,

unpaired t-test), but not in HNC010 cetuximab-resistant xenografts, in comparison with vehicle-treated xenografts (Fig.5H, p=0.13 n=5 group, unpaired t-test).

Finally, in order to further assess the metabolic shift induced by treatment with cetuximab in our three models of patient-derived tumor xenografts, mRNA expression of key enzymes and transporters of the glycolytic metabolism were analyzed by qPCR on *ex vivo* tumor samples resected from tumor bearing mice (Fig.6). The mRNA expression of lactate dehydrogenase A (LDH-A) was significantly decreased in HNC007 cetuximab-sensitive xenografts (Fig.6A, p=0.02; n= 3, 1-way ANOVA, Tukey's multiple comparison post-hoc test) and UCLHN4 cetuximab-sensitive xenografts (p=0.02, n=6, Welch's test), whereas the decrease was not significant in resistant xenografts (resistant HNC007, p=0.10, n=5; and resistant HNC010, p=0.10, n= 5; Welch's test). The mRNA expression of the lactate transporter MCT-1 (Fig.6 D,E,F) significantly decreased in cetuximab-sensitive xenografts (sensitive HNC007, p=0.017, n= 3, 1-way ANOVA, Tukey's multiple comparison post-hoc test; and sensitive UCLHN4, p=0.0031, n= 4, Welch's test) whereas the decrease was not significant in resistant xenografts (resistant HNC007, p=0.126 , n=5, 1-way ANOVA, Tukey's multiple comparison post-hoc test; and resistant HNC010, p=0.0789, n= 5, Welch's test). However, the protein levels of LDH-A was not mirroring the changes in mRNA levels, that were assessed *ex vivo* by WB analysis. With respect to MCT1, mRNA levels and IHC staining showed a significant decrease in the UCLHN4 sensitive model, contrarily to the HNC010 resistant model (p=0.015 and p=0.51, respectively, Welch's test). The mRNA expression of the glucose transporter GLUT-1 (Fig.6 G,H,I), converting glucose into 2-deoxy-glucose inside the cell, showed a non-significant decrease in cetuximab-sensitive xenografts in comparison with control tumors, but WB analysis of GLUT-1 activity (sup Fig.1) showed a significant decrease in the cetuximab-sensitive tumor model UCLHN4, and was not modified in the cetuximab-resistant HNC010 model. However, this pattern was not confirmed in the HNC007 model. Hexokinase

2 (HK2) mRNA expression (Fig.6 J,K,L) was not modified under any of the conditions, whereas the HK2 protein levels was decreased in the cetuximab-sensitive UCLHN4 model only.

**Discussion**

The three HNSCC patient-derived tumor xenograft models that we implemented for the current study involving cetuximab-sensitive and cetuximab-resistant xenografts were used for assessing metabolic imaging as a potential marker of response and resistance to the EGFR inhibitor cetuximab in head and neck cancer. Using state-of-the-art metabolic imaging, we performed the first *in vivo* assessment of cetuximab-induced metabolic changes in cetuximab-sensitive HNSCC xenografts using HP MRI. In the literature, most preclinical cancer studies using HP pyruvate as a biomarker have shown increased conversion to HP lactate, consistent with the elevated lactate production (Warburg effect) that is an established characteristic of most cancerous cells (28, 29). These studies also demonstrated a mechanistic link between an increased HP lactate signal and other cancer-associated cellular alterations such as the elevated expression of LDHA and monocarboxylate transporters (28,28,36). Importantly, in the current study, real-time monitoring of pyruvate-lactate exchange *in vivo*, estimated via the $^{13}$C-lactate to $^{13}$C-pyruvate ratio (37), was also able to distinguish between sensitive and resistant xenografts, and suggested a recovery of the glycolytic metabolism in resistant tumors, indicated by a higher rate of conversion from pyruvate to lactate, as observed in control untreated tumors. Hyperpolarized $^{13}$C-pyruvate to $^{13}$C-lactate conversion was indeed significantly decreased *in vivo* in cetuximab-sensitive xenografts 8 days after weekly treatment with cetuximab, whereas it was not modified in cetuximab-resistant xenografts using a similar protocol.

*Ex vivo* analysis of the mRNA expression and protein levels of the glycolytic pathway of tumors resected at day 8 post-treatment corroborated the *in vivo* metabolic data in the

sensitive UCLHN4 and resistant HNC010 models. Compared to control tumors, we observed a lack of change in the LDH-A enzyme expression involved in the conversion of pyruvate into lactate, but a significant decrease in the expression of the lactate transporter MCT-1 (as observed by MCT-1 IHC staining), likely to participate in the decrease in the observed lactate to pyruvate ratio *in vivo*. The significant decrease observed in UCLHN4 cetuximab-sensitive tumors was not present in the cetuximab-resistant HNC010 tumors. With respect to glycolysis, *ex vivo* analysis of the UCLHN4 cetuximab-sensitive model suggested a decrease of the glycolytic phenotype in cetuximab-treated tumors (corroborated by significant decreases in GLUT-1 and HK2 protein levels) that was not observed in the cetuximab-resistant HNC010 tumors. However, this pattern could not be confirmed in the HNC007 model. It is noteworthy that the HNC007 and UCLHN4 sensitive models originate from two different patients: the first had been treated with cetuximab in the clinic whereas the second was naïve to cetuximab. Also, resistance in the HNC007 model was generated in mice whereas the HNC010 model was intrinsically resistant in patients. Therefore, a straightforward comparison between the models is limited by the different backgrounds of the models. Further studies on larger PDTX cohorts would be required to fully characterize the metabolic changes induced by cetuximab in sensitive and resistant tumors accompanying the changes observed with metabolic imaging. Finally, the potential role of GLUT-3 and GLUT-4 should be considered in the context of HNSCC, as recently suggested by Feitosa et al. (38).

Tumor cellularity assessed by diffusion MRI was significantly increased at day 8 post-treatment in cetuximab-sensitive HNC007 xenografts when compared to pre-treatment ADCw values, but was not different for control and treated tumors at day 8. In both the HNC007 and HNC010 models, the ADCw parameter was able to distinguish cetuximab-sensitive and resistant xenografts. However, longitudinal monitoring of ADCw between day 0 and day 8 did not show any significant change in the UCLHN4 model. This is in accordance with

previous data from our group (23), in which we showed that ADCw was able to discriminate between sensitive and resistant tumors in one model but not in all models (Fig.2, ref 23). Nevertheless, it is important to keep in mind that ADCw values may be tumor-type specific and further studies should be conducted to establish the relevance of this marker in response to cetuximab. In this study, $^{13}$C-pyruvate-lactate exchange was able to indicate tumor response in this model, in accordance with tumor size stabilization and decrease in pEGFR. Accordingly, both $^{13}$C-pyruvate-lactate exchange and ADCw were able to assess response or resistance to cetuximab in all models; however, only $^{13}$C-pyruvate-lactate exchange was able to assess response/resistance longitudinally (i.e. when comparing D0 and D8 post-treatment) in all models, suggesting that the assessment of metabolic changes could be more suitable for assessing clinically relevant longitudinal response to the EGFR inhibitor in HNSCC.

Metabolic imaging using hyperpolarized $^{13}$C-pyruvate has recently been introduced into the clinical setting for prostate cancer patients (30). This study shows the potential added value of metabolic imaging for translational purposes. The study of pyruvate-lactate exchange provides the unique ability to assess metabolic changes in real time and to assess the relevance of combining EGFR inhibition with potential new targeted therapies, paving the way for future testing of combination therapies involving metabolically targeted therapies with EGFR inhibitors in HNSCC in order to counteract cetuximab-acquired or native resistance.

## Conclusion

This proof of concept study constitutes the first *in vivo* assessment of cetuximab-induced inhibition of pyruvate to lactate conversion in cetuximab-sensitive HNSCC patient-derived xenografts using state-of-the-art metabolic imaging. Importantly, the real-time monitoring of pyruvate-lactate exchange suggested a recovery of the glycolytic phenotype in cetuximab-resistant xenografts, thereby identifying hyperpolarized $^{13}$C-pyruvate as a potential marker for

response and resistance to the EGFR inhibitor in HNSCC. Further studies are however required to definitely establish the link between the changes in pyruvate to lactate conversion, metabolic changes, and sensitivity or resistance to EGFR inhibitors in HNSCC.

## Acknowledgments

This study was supported by grants from the Belgian National Fund for Scientific Research (FNRS), the "Actions de Recherches Concertées-Communauté Française de Belgique-ARC 09/14-020". BF Jordan is Research Director, PD Cani is Senior Research Associate, and C Corbet is Research Associate; of the Belgian National Fund for Scientific Research (FNRS). S Acciardo is a Televie researcher and F Gourgue is a FRIA grant holder. We thank Michele de Beukelaer from the 2IP imaging platform of UCLouvain for technical assistance.

**References**

1. Rubin Grandis J, Melhem MF, Gooding WE, Day R, Holst VA, Wagener MM, et al. Levels of TGF-alpha and EGFR protein in head and neck squamous cell carcinoma and patient survival. J Natl Cancer Inst 1998; 90(11):824-832.
2. Ang KK, Berkey BA, Tu X, Zhang HZ, Katz R, Hammond EH, et al. Impact of epidermal growth factor receptor expression on survival and pattern of relapse in patients with advanced head and neck carcinoma. Cancer Res 2002; 62(24):7350-7356.
3. Bonner JA, Harari PM, Giralt J, Azarnia N, Shin DM, Cohen RB, et al. Radiotherapy plus cetuximab for squamous-cell carcinoma of the head and neck. N Engl J Med 2006; 354(6):567-578.
4. Vermorken JB, Mesia R, Rivera F, Remenar E, Kawecki A, Rottey S, et al. Platinum-based chemotherapy plus cetuximab in head and neck cancer. N Engl J Med 2008; 359(11):1116-1127.
5. Bentzen SM, Atasoy BM, Daley FM, Dische S, Richman PI, Saunders MI, et al. Epidermal growth factor receptor expression in pretreatment biopsies from head and neck squamous cell carcinoma as a predictive factor for a benefit from accelerated radiation therapy in a randomized controlled trial. J Clin Oncol 2005; 23(24):5560-5567.
6. Machiels JP, Subramanian S, Ruzsa A, Repassy G, Lifirenko I, Flygare A, et al. Zalutumumab plus best supportive care versus best supportive care alone in patients with recurrent or metastatic squamous-cell carcinoma of the head and neck after failure of platinum-based chemotherapy: an open-label, randomised phase 3 trial. Lancet Oncol 2011; 12(4):333-343.

7. Cohen RB. Current challenges and clinical investigations of epidermal growth factor receptor (EGFR)- and ErbB family-targeted agents in the treatment of head and neck squamous cell carcinoma (HNSCC). Cancer Treat Rev. 2014;40(4):567-77.
8. Wheeler DL, Dunn EF, Harari PM. Understanding resistance to EGFR inhibitors-impact on future treatment strategies. Nat Rev Clin Oncol. 2010;7(9):493-507.
9. Rabinowits G, Haddad RI. Overcoming resistance to EGFR inhibitor in head and neck cancer: a review of the literature. Oral Oncol. 2012;48(11):1085-9.
10. Silva-Oliveira RJ, Melendez M, Martinho O, Zanon MF, de Souza Viana L, Carvalho AL et al. AKT can modulate the in vitro response of HNSCC cells to irreversible EGFR inhibitors. Oncotarget. 2017;8(32):53288-53301.
11. De Pauw I, Lardon F, Van den Bossche J, Baysal H, Fransen E, Deschoolmeester V, et al. Simultaneous targeting of EGFR, HER2, and HER4 by afatinib overcomes intrinsic and acquired cetuximab resistance in head and neck squamous cell carcinoma cell lines. Mol Oncol. 2018;12(6):830-854.
12. Cohen RB. Current challenges and clinical investigations of epidermal growth factor receptor (EGFR)- and ErbB family-targeted agents in the treatment of head and neck squamous cell carcinoma (HNSCC). Cancer Treat Rev. 2014;40(4):567-77.
13. Graham J, Muhsin M, Kirkpatrick P. Cetuximab. Nat Rev Drug Discov. 2004 ;3(7):549-50.
14. Cohen EE, Lingen MW, Martin LE, Harris PL, Brannigan BW, Haserlat SM et al. Response of some head and neck cancers to epidermal growth factor receptor tyrosine kinase inhibitors may be linked to mutation of ERBB2 rather than EGFR. Clin Cancer Res 2005;11(22):8105–8.

15. Loeffler-Ragg J, Witsch-Baumgartner M, Tzankov A, Hilbe W, Schwentner I, Sprinzl GM et al. Low incidence of mutations in EGFR kinase domain in Caucasian patients with head and neck squamous cell carcinoma. Eur J Cancer 2006;42(1):109–11.
16. Licitra L, Mesia R, Rivera F, Remenar E, Hitt R, Erfan J, et al. Evaluation of EGFR gene copy number as a predictive biomarker for the efficacy of cetuximab in combination with chemotherapy in the first-line treatment of recurrent and/or metastatic squamous cell carcinoma of the head and neck: EXTREME study. Ann Oncol 2011;22(5):1078–87.
17. Fountzilas G, Kalogera-Fountzila A, Lambaki S, Wirtz RM, Nikolaou A, Karayannopoulou G et al. MMP9 but not EGFR, MET, ERCC1, P16, and P-53 is associated with response to concomitant radiotherapy, cetuximab, and weekly cisplatin in patients with locally advanced head and neck cancer. J Oncol 2009;2009:305908.
18. Kishimoto S, Oshima N, Krishna MC, Gillies RJ. Direct and indirect assessment of cancer metabolism explored by MRI. NMR Biomed 2018:e3966.
19. Liu FY, Yen TC, Wang JY, Yang TS. Early prediction by 18F-FDG PET/CT for progression-free survival and overall survival in patients with metastatic colorectal cancer receiving third-line cetuximab-based therapy. Clin Nucl Med 2015;40(3):200-5.
20. Winther-Larsen A, Fledelius J, Demuth C, Bylov CM, Meldgaard P, Sorensen BS. Early Change in FDG-PET signal and plasma cell-free DNA level predicts erlotinib response in EGFR wild-type NSCLC patients. Transl Oncol 2016;9(6):505-511.
21. Sohn H, Yang Y, Ryu J, Oh S, Im K, Moon D, et al. [18F] Fluorothymidine positron emission tomography before and 7 days after gefitinib treatment predicts response in patients with advanced adenocarcinoma of the lung. Clin Cancer Res 2008;14:7423–7429.

22. Baker LCJ, Sikka A, Price JM, Boult JKR, Lepicard EY, Box G, et al. Evaluating Imaging Biomarkers of Acquired Resistance to Targeted EGFR Therapy in Xenograft Models of Human Head and Neck Squamous Cell Carcinoma. Front Oncol. 2018 23;8:271.
23. Mignion L, Schmitz S, Michoux N, Caignet X, Goebbels RM, Bol A, et al. 2'-deoxy-2'-[18F] fluoro-D-glucose positron emission tomography, diffusion-weighted magnetic resonance imaging, and choline spectroscopy to predict the activity of cetuximab in tumor xenografts derived from patients with squamous cell carcinoma of the head and neck. Oncotarget. 2018;9(47):28572-28585.
24. Lu H, Li X, Luo Z, Liu J, Fan Z. Cetuximab reverses the Warburg effect by inhibiting HIF-1-regulated LDH-A. Mol Cancer Ther. 2013;12(10):2187-99.
25. Li X, Lu Y, Lu H, Luo J, Hong Y, Fan Z. AMPK-mediated energy homeostasis and associated metabolic effects on cancer cell response and resistance to cetuximab. Oncotarget. 2015;6(13):11507-18.
26. Luo J, Hong Y, Lu Y, Qiu S, Chaganty BK, Zhang L, et al. Acetyl-CoA carboxylase rewires cancer metabolism to allow cancer cells to survive inhibition of the Warburg effect by cetuximab. Cancer Lett. 2017;384:39-49.
27. Ardenkjaer-Larsen JH, Fridlund B, Gram A, Hansson G, Hansson L, Lerche MH, et al. Increase in signal-to-noise ratio of > 10,000 times in liquid-state NMR. Proc Natl Acad Sci U S A 2003;100:10158-63.
28. Hesketh RL, Brindle KM. Magnetic resonance imaging of cancer metabolism with hyperpolarized 13C-labeled cell metabolites. Curr Opin Chem Biol. 2018;45:187-194.
29. Scroggins BT, Matsuo M, White AO, Saito K, Munasinghe JP, Sourbier C, et al. Hyperpolarized [1-13C]-Pyruvate Magnetic Resonance Spectroscopic Imaging of

Prostate Cancer In Vivo Predicts Efficacy of Targeting the Warburg Effect. Clin Cancer Res. 2018;24(13):3137-3148. doi: 10.1158/1078-0432.CCR-17-1957.

30. Nelson SJ, Kurhanewicz J, Vigneron DB, Larson PE, Harzstark AL, Ferrone M, et al. Metabolic imaging of patients with prostate cancer using hyperpolarized [1-13C]pyruvate. Sci Transl Med 2013;5:198ra108
31. Miloushev VZ, Granlund KL, Boltyanskiy R, Lyashchenko SK, DeAngelis LM, Mellinghoff IK, et al. Metabolic Imaging of the Human Brain with Hyperpolarized 13C Pyruvate Demonstrates 13C Lactate Production in Brain Tumor Patients. Cancer Res. 2018;78(14):3755-3760.
32. Kurhanewicz J, Vigneron DB, Ardenkjaer-Larsen JH, Bankson JA, Brindle K, Cunningham CH, Gallagher FA, Keshari KR, Kjaer A, Laustsen C, Mankoff DA, Merritt ME, Nelson SJ, Pauly JM, Lee P, Ronen S, Tyler DJ, Rajan SS, Spielman DM, Wald L, Zhang X, Malloy CR, Rizi R. Hyperpolarized 13C MRI: Path to Clinical Translation in Oncology. Neoplasia. 2019 ;21(1):1-16. doi: 10.1016/j.neo.2018.09.006.
33. Afaq A, Andreou A and Koh D.M. Diffusion-weighted magnetic resonance imaging for tumour response assessment: why, when and how? Cancer Imaging 2010; 10(1A): S179–S188.
34. King A and Thoeny HC. Functional MRI for the prediction of treatment response in head and neck squamous cell carcinoma: potential and limitations. Cancer imaging 2016; 16:23.
35. Heijmen L, Verstappen M, Voert E, Punt C, Oyenc W, de Geus-Oei LF, et al. Tumour response prediction by diffusion-weighted MR imaging: Ready for clinical use? Critical Reviews in Oncology/Hematology 2012;83:194–207.

36. Corbet C, Bastien E, Draoui N, Doix B, Mignion L, Jordan BF, Marchand A, Vanherck JC, Chaltin P, Schakman O, Becker HM, Riant O, Feron O. Interruption of lactate uptake by inhibiting mitochondrial pyruvate transport unravels direct antitumor and radiosensitizing effects. Nat Commun. 2018;9(1):1208.

37. Witney TH, Kettunen MI. & Brindle, K. M. Kinetic modeling of hyperpolarized 13C label exchange between pyruvate and lactate in tumor cells. J. Biol. Chem. 2011;286:24572–24580.

38. Feitosa SG, Viana KF, Luna ECM, Gurgel Costa FW, Cavalcante RB, Nobre Chaves F, Vasconcelos Chaves H, Alves Pereira KM. Immunohistochemical Evaluation of GLUT-3 and GLUT-4 in Oral Epithelial Dysplasia and Oral Squamous Cell Carcinoma. Asian Pac J Cancer Prev. 2018; 19(7): 1779–1783.

## Figure legends

**Figure 1. Tumor growth of HNC007 PDTX.** (**A**) Tumor growth of cetuximab-sensitive HNC007 tumors treated with cetuximab (30 mg/kg IP, once a week) vs control tumors (saline solution IP, once a week) (**B**) Evolution of tumor volume between baseline (D0) and day 8 (D8) (corresponding to the timeframe of the imaging experiments) in HNC007 control mice (saline solution IP, once a week). (**C**) Evolution of tumor volume between D0 and D8 in cetuximab-sensitive HNC007 mice treated with cetuximab (30 mg/kg IP, once a week). (**D**) Tumor growth of cetuximab-resistant HNC007 PDTX (acquired resistance induced by treatment with cetuximab, 30 mg/kg IP, once a week). Xenografts were considered resistant when tumors reached 200% +/- 10% of their initial size. (**E**) Evolution of the tumor volume between D0 and D8 in cetuximab-resistant HNC007 PDTX treated with cetuximab (30 mg/kg IP, once a week). (**F**) Multiple comparison of the evolution of tumor volumes between D0 and D8 in control (vehicle), cetuximab-sensitive (treated with cetuximab) and cetuximab-resistant (treated with cetuximab) HNC007 PDTX.

**Figure 2. pEGFR histoscore (Box Plot) of HNC007 PDTX** (harvested on day 8 after sacrifice of the mice used in the imaging experiments). (**A**) Control: HNC007 control mice treated with saline solution (IP, once a week); Cetuximab sensitive HNC007: HNC007 mice treated with cetuximab on day 0 and 7 (30 mg/kg IP); Cetuximab resistant HNC007: HNC007 mice treated with cetuximab on day 0 and 7 (30 mg/kg IP); (**B**) typical pEGFR IHC staining in untreated HNC007 tumor (up), in sensitive HNC007 (middle) and in resistant HNC007 (bottom) tumor treated with cetuximab on day 0 and 7 (30 mg/kg IP).

**Figure 3. Evolution of the $^{13}$C lactate/$^{13}$C pyruvate ratio after treatment with cetuximab in HNC007 PDTX.** (**A**) Typical $^{13}$C-MRS spectra acquired *in vivo* from HNC007 PDTX at baseline (D0) before any treatment; (**B**) Evolution of $^{13}$C-pyruvate and $^{13}$C-lactate peaks over time (200s acquisition) before and after 8 days (D8) of weekly cetuximab treatment in a typical cetuximab-sensitive HNC007 PDTX; (**C**) Evolution of the $^{13}$C lactate/$^{13}$C pyruvate ratio between D0 and D8 in HNC007 control PDTX (weekly vehicle IP injection); (**D**) Evolution of the $^{13}$C lactate/$^{13}$C pyruvate ratio between D0 and D8 in cetuximab-resistant HNC007 PDTX (cetuximab 30 mg/kg IP, once a week); (**E**) Evolution of the $^{13}$C lactate/$^{13}$C pyruvate ratio between D0 and D8 in cetuximab-sensitive HNC007 PDTX (cetuximab 30 mg/kg IP, once a week); (**F**) Multiple comparisons of the evolutions of $^{13}$C lactate/$^{13}$C

pyruvate between D0 and D8 in control (vehicle), cetuximab-sensitive (treated with cetuximab) and cetuximab-resistant (treated with cetuximab) HNC007 PDTX.

**Figure 4. Tumor cellularity assessed using tumor ADCw (apparent diffusion coefficient of water) via Diffusion-MRI in HNC007 PDTX** (**A**) Typical diffusion map at baseline (D0), before any treatment, in a cetuximab-sensitive HNC007 PDTX. The color map represents tumor ADCw values overlaid on the corresponding anatomical image on a transversal slice of the tumor-bearing mouse; (**B**) Typical diffusion map on day 8 (D8), after cetuximab treatment (30 mg/kg IP, once a week) in the same cetuximab-sensitive HNC007 PDTX; (**C**) Evolution of tumor ADCw between D0 and day 8 in HNC007 control PDTX (weekly vehicle IP injection); (**D**) Evolution of ADCw between D0 and D8 in cetuximab-sensitive HNC007 PDTX, treated with cetuximab (30 mg/kg IP, once a week); (**E**) Evolution of the $ADC_w$ between D0 and D8 in cetuximab-resistant HNC007 mice treated with cetuximab (30 mg/kg IP, once a week). (**F**) Multiple comparisons of the evolution of tumor ADCw between D0 and D8 in control (vehicle), cetuximab-sensitive (treated with cetuximab) and cetuximab-resistant (treated with cetuximab) HNC007 PDTX.

**Figure 5. Evolution of tumor volume, $^{13}$C lactate/$^{13}$C pyruvate ratio, ADCw, and pEGFR histoscore before and after treatment with cetuximab in UCLHN4 cetuximab-naïve PDTX and in HN010 cetuximab primary resistant PDTX.** (**A-B**) Evolution of the tumor volume between D0 and D8 in control (weekly vehicle IP injection) and treated (cetuximab 30 mg/kg IP, once a week) (**A**) UCLHN4 cetuximab-sensitive PDTX and **(B)** HNC010 cetuximab-resistant PDTX; (**C-D**) Evolution of the $^{13}$C lactate/$^{13}$C pyruvate ratio between D0 and D8 in control (weekly vehicle IP injection) and treated (cetuximab 30 mg/kg IP, once a week) (**C)** UCLHN4 cetuximab-sensitive xenograft model and **(D)** HNC010 cetuximab-resistant PDTX; (**E-F**) Evolution of tumor ADCw between D0 and D8 in control (weekly vehicle IP injection) and treated (cetuximab 30 mg/kg IP, once a week) (**E)** UCLHN4 cetuximab-sensitive xenograft model and (**F**) HNC010 cetuximab-resistant PDTX; (**G-H**) pEGFR histoscore (Box Plot) performed on tumors harvested on day 8 after sacrifice of the mice of the (**G)** UCLHN4 cetuximab-sensitive xenograft model (**H**) HNC010 cetuximab-resistant xenograft model.

**Figure 6. mRNA expression (open symbols, left Y-axis) and protein levels (plain symbols, right Y-axis) of LDH-A, MCT-1, Glut-1, and HK2.** (**A,B,C**) Evolution of mRNA

expression and protein levels of lactate dehydrogenase A (LDH-A) in the tumor tissue harvested on day 8 after sacrifice of the mice from the three models (HNC007, UCLHN4 and HNC010). (**D,E,F**) Evolution of mRNA expression and MCT-1 IHC staining index of the lactate transporter MCT-1 in the tumoral tissue harvested on day 8 after sacrificing the mice from the three models. (**G,H,I**) Evolution of mRNA expression and protein levels of the glucose transporter GLUT-1 in the tumoral tissue harvested on day 8 after sacrificing the mice from the three models. (**J,K,L**) Evolution of mRNA expression and protein levels of Hexokinase-2 (HK2: converting glucose into 2 deoxy glucose inside the cell) in the tumoral tissue harvested on day 8 after sacrificing the mice from the three models. For each model, control mice were treated with saline solution weekly, and treated mice were treated with cetuximab (30 mg/kg IP) once a week at day 0 and 7. Cetuximab mice with acquired resistance were treated once a week; xenografts were considered resistant when tumors reached 200% +/- 10% of their initial size.

# Fig.1

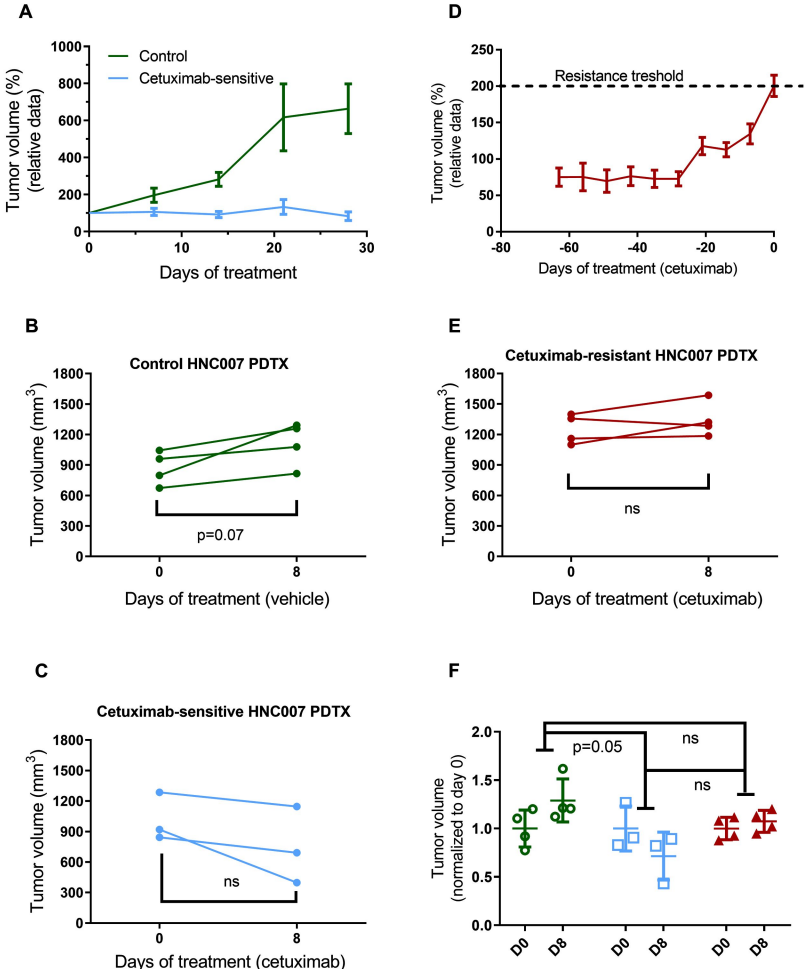

Fig.2

A

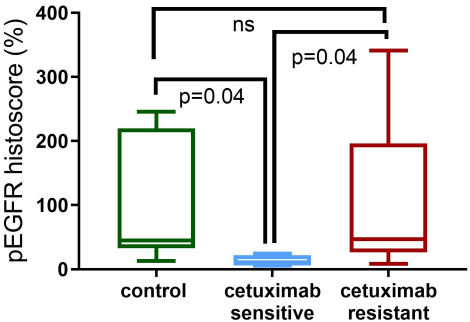


B

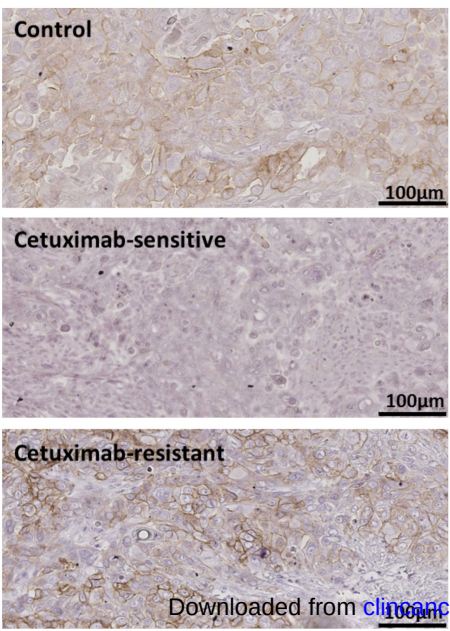

Fig.3

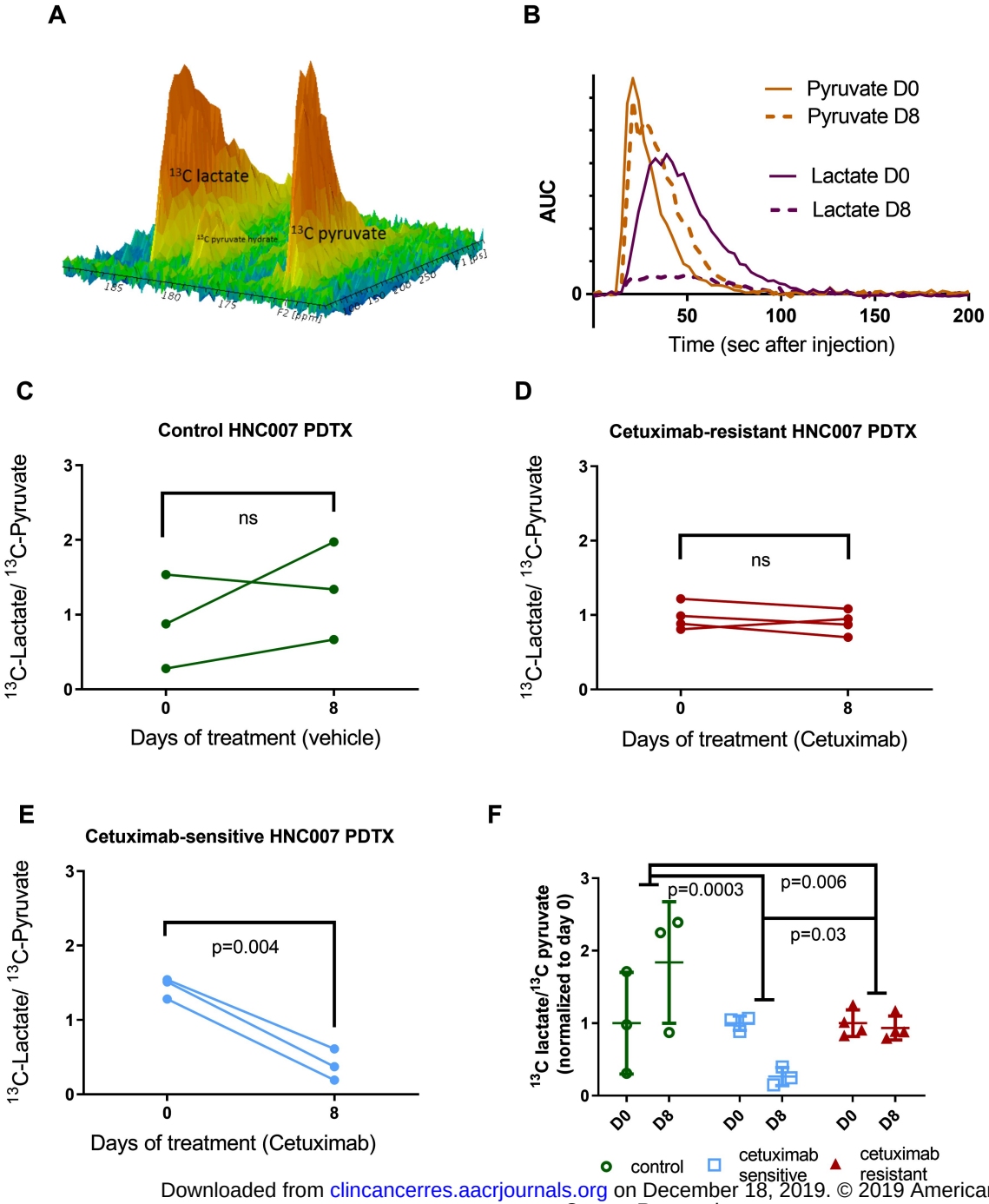

# Fig. 4

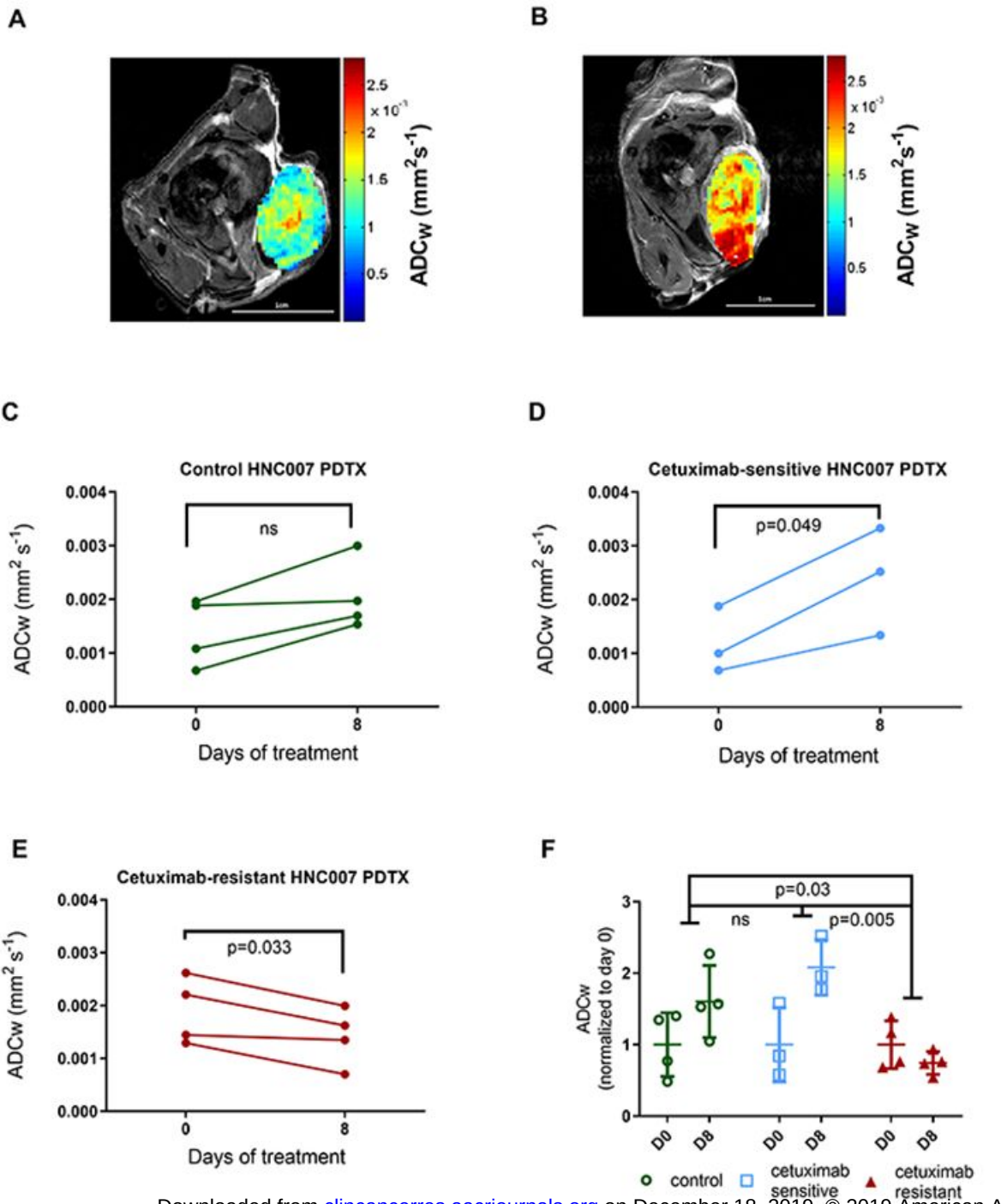

# Fig. 5

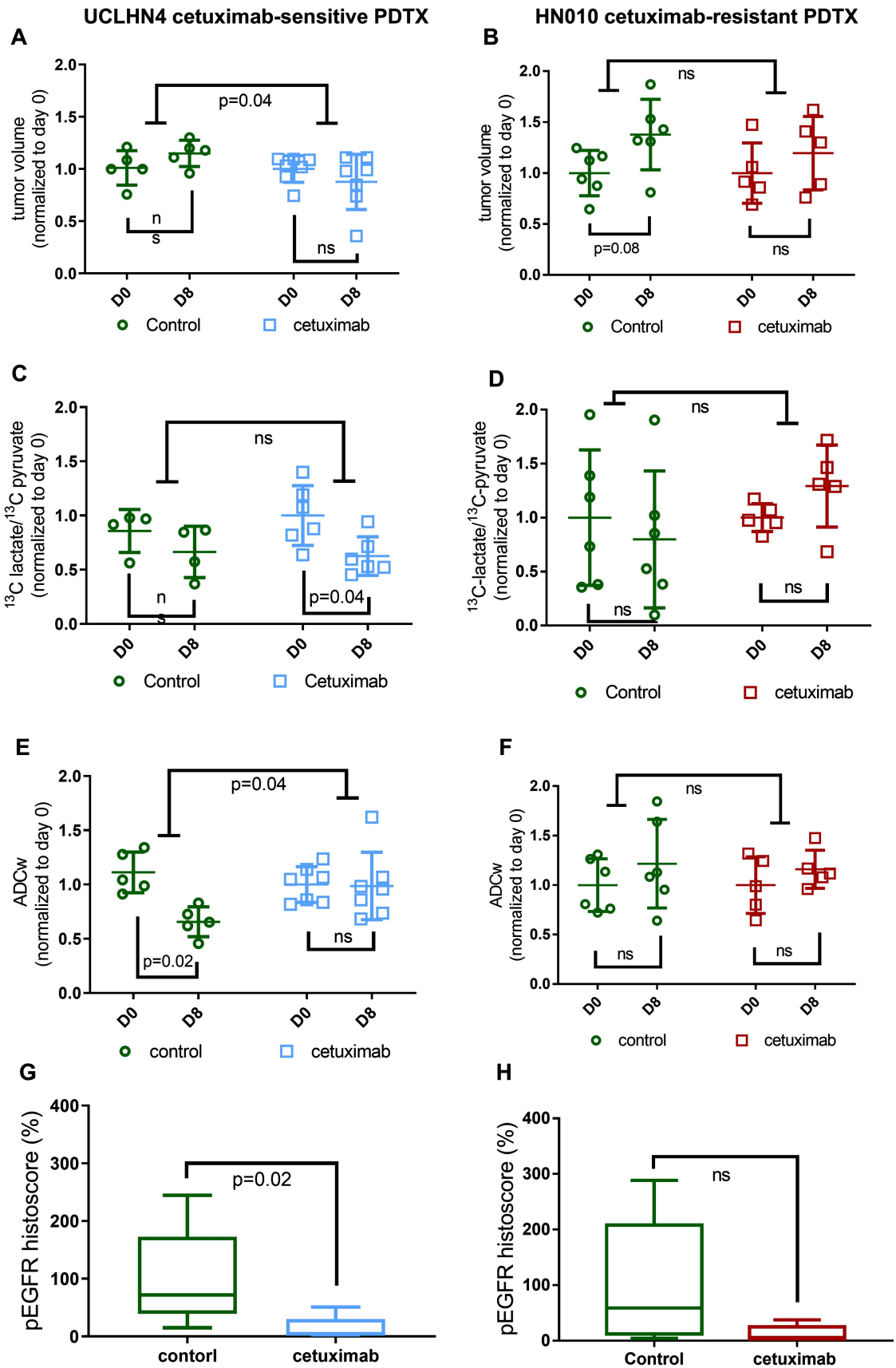

# Fig.6

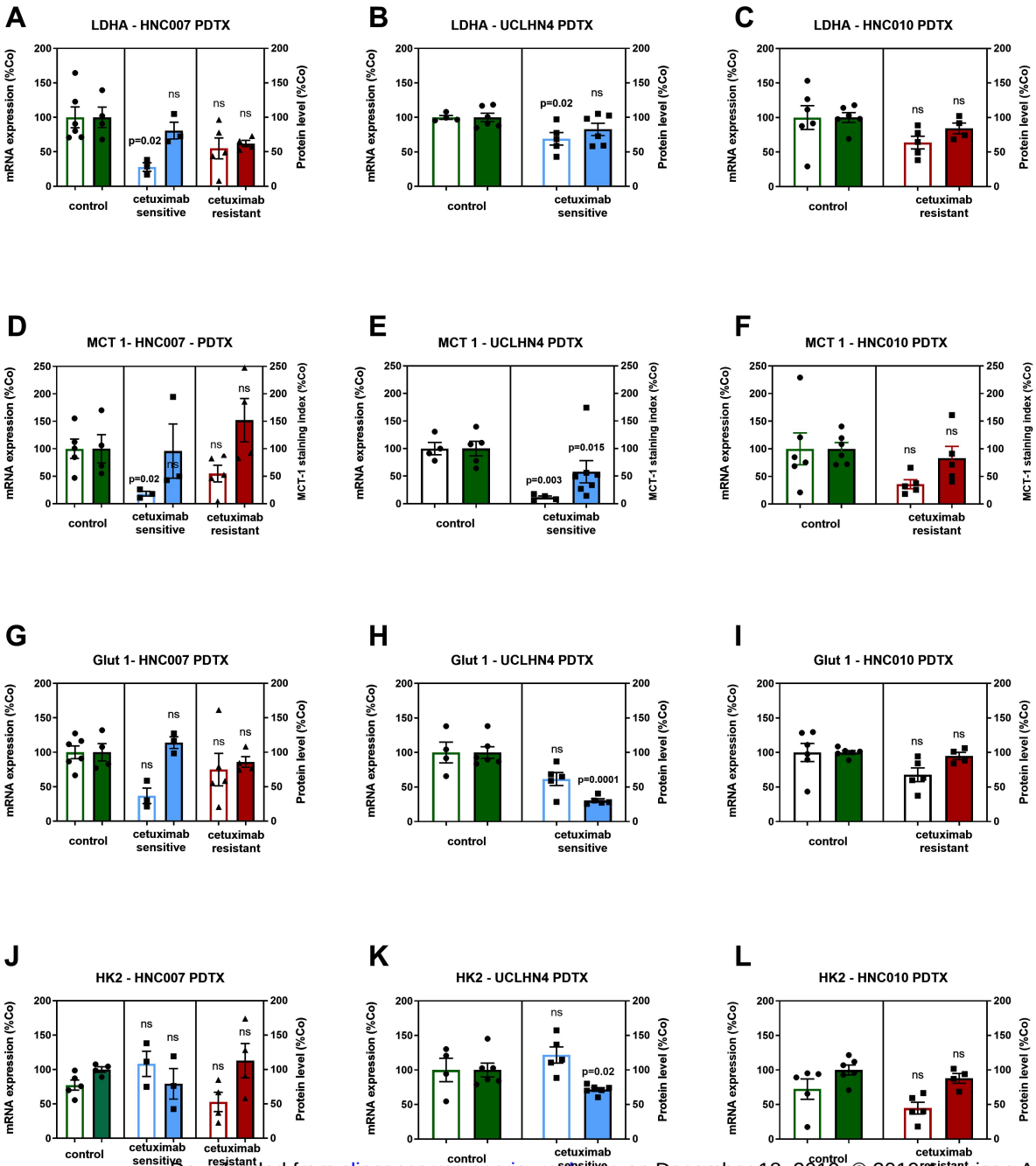

AACR American Association for Cancer Research

Clinical Cancer Research

# Metabolic imaging using hyperpolarized pyruvate-lactate exchange assesses response or resistance to the EGFR inhibitor cetuximab in patient-derived HNSCC xenografts

Lionel Mignion, Stefania Acciardo, Florian Gourgue, et al.

*Clin Cancer Res* Published OnlineFirst December 12, 2019.